Emulsion imaging of a DNA nanostar condensate phase diagram reveals valence and electrostatic effects

Nathaniel Conrad,[1] Grace Chang,[1, a)] Deborah K. Fygenson,[1, 2] and Omar A. Saleh[1, 2, 3]

[1)]*Department of Physics, University of California, Santa Barbara, CA 93106*

[2)]*Department of Biomolecular Science and Engineering, University of California, Santa Barbara, CA 93106*

[3)]*Materials Department, University of California, Santa Barbara, CA 93106*

(*Corresponding authors' e-mail: nconrad@ucsb.edu, fygenson@ucsb.edu, saleh@ucsb.edu)

(Dated: 1 December 2022)

Liquid-liquid phase separation (LLPS) in macromolecular solutions (e.g. coacervation) is relevant both to technology, and to the process of mesoscale structure formation in cells. The LLPS process is characterized by a phase diagram, i.e. binodal lines in the temperature/concentration plane, which must be quantified to predict the system's behavior. Experimentally, this can be difficult due to complications in handling the dense macromolecular phase. Here, we develop a method for accurately quantifying the phase diagram without direct handling: We confine the sample within micron-scale, water-in-oil emulsion droplets, then use precision fluorescent imaging to measure the volume fraction of the condensate within the droplet. We find this volume fraction grows linearly with macromolecule concentration; thus, by applying the lever rule, we can directly extract the dense and dilute binodal concentrations. We use this approach to study a model LLPS system of self-assembled, fixed-valence DNA particles termed nanostars (NSs). We find that temperature/concentration phase diagrams of NSs display, with certain exceptions, a larger co-existence regime upon increasing salt or valence, in line with expectations. Aspects of the measured phase behavior validate recent predictions that account for the role of valence in modulating the connectivity of the condensed phase. Generally, our results on NS phase diagrams give fundamental insight into limited-valence phase separation, while the method we have developed will likely be useful in the study of other LLPS systems.

[a)]Now at: Department of Biomedical Engineering, University of Pennsylvania, Philadelphia, PA 19104

I. INTRODUCTION

Liquid-liquid phase separation (LLPS) of aqueous solutions of macromolecules involves the equilibrium segregation of a fluid into regions dense in macromolecule, and regions dilute in macromolecule. The process has long been studied in mixtures of oppositely charged polymers, where it is termed complex coacervation[1]. Investigating the variables which control macromolecular LLPS is critical to further both our understanding of its role in biological systems[2–7] and development of tunable materials for pharmaceutical or food-science applications[8–12].

The LLPS process is generally controlled by temperature, the concentration of the macromolecule and of other solutes (e.g. salt), and the nature of the interactions in the system, including with the solvent[13,14]. Fundamental to the characterization of LLPS, and its sensitivity to such parameters, is the equilibrium phase diagram, in which binodal lines separate the conditions in which an equilibrated solution will form a single, homogeneous fluid, from those in which the solution will spontaneously separate into coexisting dense and dilute phases. Experimental measurements of binodal lines are made challenging by the need to handle and assay each phase. The most common method involves separating the dilute and dense phases by centrifugation[13–15], which typically requires large volumes of solution ($\gtrsim$ 100 μL) that may be inaccessible and/or prohibitively expensive[16] for some systems. Further, dense macromolecular phases are typically highly viscous, and prone to adhere to solid surfaces, making handling difficult.

The difficulties in working with phase-separating systems can be ameliorated by encapsulating them within the aqueous droplets of water-in-oil emulsions. Indeed, as demonstrated in prior works[17–19], the emulsion approach has advantages, including (i) not involving centrifugation or direct handling of the phase-separated solution, (ii) requiring small amounts of the solution of interest, and (iii) being agnostic to the macromolecule under investigation. Here, we exploit these advantages to develop an emulsion-based fluorescent imaging method for measuring the binodal lines of macromolecular LLPS systems in the temperature-concentration plane. We confine the system of interest in micron-scale, water-in-oil emulsion droplets, and then image the droplets using a temperature-controlled, wide-field fluorescence microscope equipped with a low numerical aperture, low magnification lens. The images capture the full fluorescent profile of an emulsion droplet, which we can fit to the expected profile, resulting in precise quantification of the volume fraction of the dense phase. We then use the measured concentration-dependence of the volume fraction, and the lever rule of binary, equilibrium phase separation[13,20], to estimate the binodal

concentrations of the respective phases. Independently, we measure the melting temperature by visualizing the appearance of condensate within the emulsion droplet while scanning temperature. Together, the measured melting temperatures and binodal concentrations allow us to construct the full phase diagram.

We use this method to investigate the phase behavior of floppy, multi-valent DNA nanostructures, called nanostars (NSs), that exhibit LLPS[15,21]. NSs are self-assembled nanostructures in which a well-defined number, f, of double-stranded DNA arms emanate from a single, flexible junction[15]. A short single-stranded DNA sequence at the distal end of the arms, known as a sticky-end, can mediate NS-NS binding through DNA basepairing. The programmable nature of sequence-controlled DNA self-assembly allows facile modulation of f, opening up an avenue to explore how valence affects solution dynamics and viscoelasticity[15,22–28]. Here, we use emulsion imaging to explore how NS phase diagrams change as f increases from 3 to 6, and we test how $f = 3$ and 4 NS phase diagrams are affected by added monovalent salt. We interpret our results with respect to structures and physical mechanisms that are expected to affect NS density, and also carry out a quantitative comparison of our data to theoretical models of NS phase separation[26], notably validating valence-sensitive predictions for the critical temperature.

Generally, the work presented here presents a method for quantifying LLPS phase diagrams that avoids issues in prior approaches, and is thus of potentially broad utility. Further, our application of the method to the NS system gives insight into the principles guiding phase separation of multivalent particles.

II. METHODS

A. Preparation of NSs and emulsions

A full description of all methods can be found in the Appendices. Briefly, we prepared f-armed NSs by mixing together equimolar amounts of f single-stranded DNA oligomers designed to self-assemble into a NS upon annealing (Fig. 1A; DNA sequences given in supplementary material, Table S1). A fraction of the oligos were tagged with a fluorescent molecule for later visualization (see Appendix A). We also separately annealed a non-interacting, fluorescently-tagged DNA hairpin and added it to the NS solution at 5 μM (Fig. 1A). The hairpin was added to brighten the dilute phase so that it could be visualized alongside the dense phase, which is typically

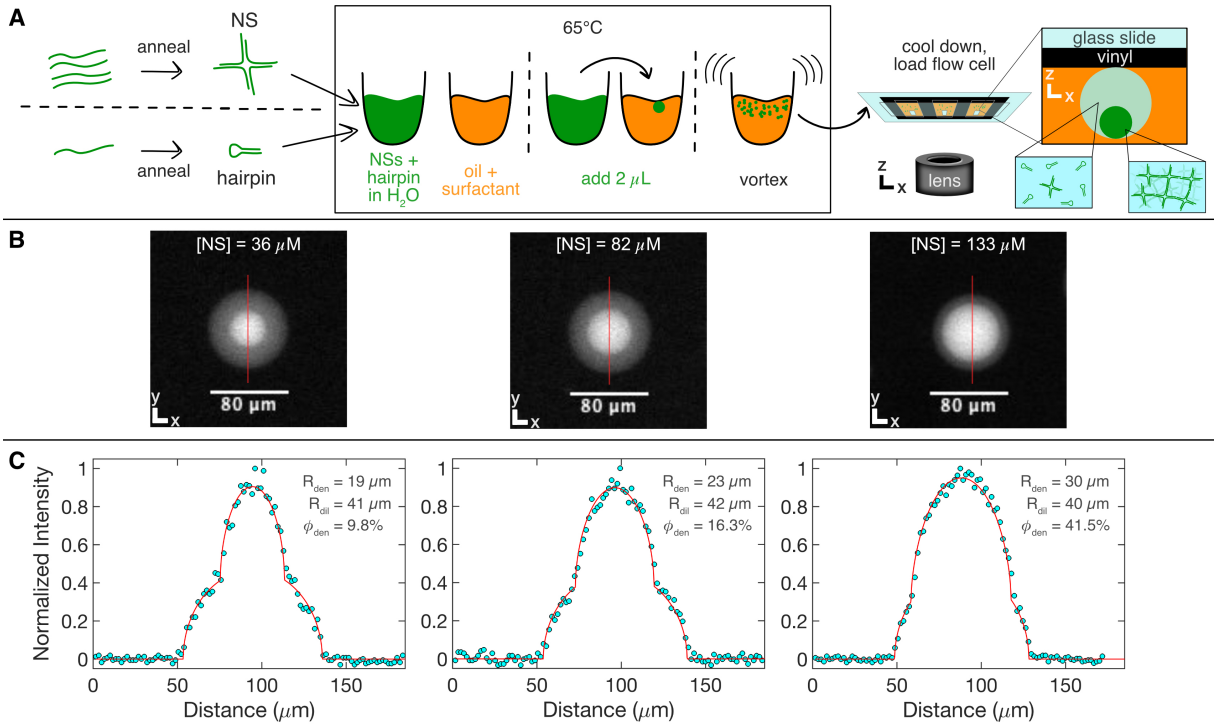

FIG. 1. **(A)** Schematic depicting the preparation of samples for emulsion-imaging of NS phase diagrams; see also Appendix A. NSs and non-interacting hairpins are annealed separately and mixed together. Then, 2-3 μL of aqueous NS+hairpin solution is added to ≈ 40 μL of an oil/surfactant mixture and briefly vortexed to create water-in-oil emulsion droplets. The sample is loaded into a flow cell, and cooled, allowing the NSs to phase separate, forming a dense, spherical DNA liquid drop within the spherical emulsion droplets. **(B)** Representative images of emulsion droplets containing phase-separated 4 arm NS solutions (150 mM NaCl, $T = 33.1 \pm 0.5^{\circ}C$), at different total NS concentrations, [NS], as labeled. The red lines depict the positions of the 1-d intensity profiles shown in panel C. Each image shown was cropped from a larger field of view; in practice, we typically analyzed 5-10 droplets per field of view (Appendix B; see also supplementary material, Fig. S2). **(C)** Profile of image intensity along the pixels indicated in panel B (cyan), along with the best-fit line (red) for the double-sphere function (supplementary material, Section S1). Labels indicate the best-fit radii, which have a fit uncertainty of ≈ 0.01-0.02 μm.

$\approx$100-1000x more concentrated. NS phase separation was unaffected by moderate amounts of hairpin (see supplementary material, Fig. S3). The concentrations of both NS and hairpin were measured using UV absorbance.

We made water-in-oil emulsions by adding 2-3 μL of the NS+hairpin solution to 40 μL of an oil and surfactant mixture, which was kept warm ($T \approx 65^{\circ}$C) to prevent NS phase separation, then

vortexing for 2-3 seconds (see Appendix A). The resulting emulsion droplets had diameters of $\approx 25 - 120\ \mu$m, as appropriate for our microscopic approach.

We placed emulsified NS solutions, each prepared with a different concentration of nanostars, [NS], into separate channels of a custom-built multi-channel flow cell (see Appendix B). The flow cell was then placed on a temperature-controlled microscopic stage, and allowed to equilibrate. NS phase separation occurred within the emulsion droplets as they cooled (Fig. 1B). The dense NS phase equilibrated into a sphere inside the aqueous emulsion droplet, as expected given its liquid-like nature[22] and consistent with previous experiments on NSs undergoing LLPS[21]. The water droplet, being less dense than the oil, rose (creamed) to the top of the flow cell, while the NS condensate, being heavier than water[21], settled to the bottom of its water droplet container (Fig. 1A).

B. Measurement of condensate melting temperature

To estimate the melting temperature, T_m, of the dense phase at a given [NS], we recorded a video of emulsion droplets while slowly raising and lowering the temperature of the stage (typically 0.5°C/min; see supplementary material, Fig. S6). Because it was difficult to identify a single frame at which the condensate appeared or disappeared, we estimated T_m as the average T over the range of frames – from the first/last frame in which a phase boundary was clearly present to the last/first frame in which it was clearly absent – and used the range of T to estimate the uncertainty in T_m. This procedure was also used in the few cases in which there was significant hysteresis (typically of 2-6°C).

C. Measurement of condensate volume fraction

At a given T and [NS], we measured the volume fraction of the dense phase, ϕ_{den}, by imaging the emulsion droplets using a low numerical aperture (0.1 or 0.13 NA), low magnification (4x) objective. Typical images and intensity profiles are shown in Fig. 1 and supplementary material, Fig. S2. The use of low NA optics imparted on the imaging system a large depth-of-field, so a single image (properly focused) captured all fluorescent intensity within a water droplet. The act of imaging thus projected, into the 2-d image, a 3-d fluorescent "double-sphere" corresponding to the smaller, bright sphere of dense NS liquid, and the larger, dimmer dilute NS solution contained in

the spherical emulsion. Correspondingly, we found that the emulsion droplets' 2-d intensity profiles, $I(x,y)$, were consistently well fit ($R^2 \geq 0.99$) by a geometric function for the two-dimensional projection of two spheres, of differing sizes and intensities (Fig. 1C; also see supplementary material, Section S1 and Fig. S1). The fitting parameters were the radii R of the emulsion droplet and NS condensate; their central positions in (x,y); and the fluorescence intensity of each phase. We then found the volume fraction through $\phi_{\text{den}} = (R_{\text{den}}/R_{\text{dil}})^3$, where the subscripts denote the dense and dilute phases.

The use of low-NA optics degrades the lateral resolution of the microscope, increasing diffractive blur in the image; this blur is not described by the double-sphere fitting function. However, we found that blurring only caused very slight deviations between the data and the fit (see supplementary material, Fig. S1B), likely because the diffraction limit of the system, ≈ 3 μm, is much smaller than the size of the condensate and emulsion droplet (> 10 μm). This indicates the fit values are robust against such blurring.

To test the sensitivity of the fitting procedure to the microscope focus, we acquired and analyzed images at a variety of focal positions. We found the best-fit radii were insensitive to focal position over a broad range (120-150 μm; see supplementary material, Fig. S4), meaning that precise focus was not needed. Further, while our emulsions contained a range of droplet sizes that accordingly were located at different heights in the flow cell, the insensitivity to focal position meant that we were able to accurately analyze emulsion droplets of different diameters from a single image. Particularly, the fitted radii from a single image of multiple emulsion droplets that ranged from ≈ 25 μm to 120 μm in diameter, each containing the same NS concentration, all resulted in the same value of ϕ_{den} (supplementary material, Fig. S4).

III. RESULTS

A. The lever rule and measuring binodal concentrations

We measured ϕ_{den} vs. [NS] across a range of temperatures, $10^{\circ}\text{C} \leq T \leq 43^{\circ}\text{C}$, for a variety of NS systems with different f and/or in different concentrations of monovalent salt, [NaCl] (Fig. 2, see also supplementary material Fig. S5). In all cases, we observed that ϕ_{den} scales linearly with [NS]. This is characteristic of a binary system undergoing equilibrium phase separation[13,20], as

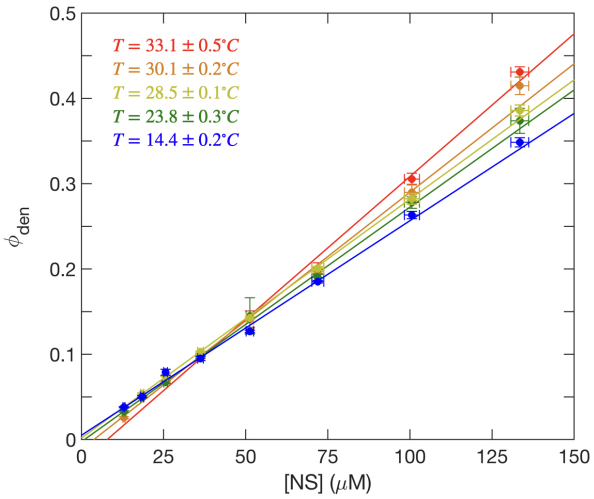

FIG. 2. The volume fraction of the dense phase, ϕ_{den}, of $f = 4$ NSs at 150 mM NaCl as a function of the total NS concentration, [NS], at various temperatures. The solid line denotes the (weighted) least squares fit of the lever rule (Eq. 1) to each data set. Lever rule plots for other salts and arm numbers are shown in the supplementary material (Fig. S5). Each plotted point corresponds to, typically, 10-30 measured droplets, with some points having as few as 2 droplets, and some as many as 50. For each temperature, at least 100 droplets are measured across all concentrations. Vertical error bars correspond to the standard error of the mean (SEM) of the fits to various droplets, while horizontal error bars correspond to the SEM of UV absorbance measurements of the NS stock concentration.

expressed by the lever rule:

$$\phi_{den} = \frac{[\text{NS}] - [\text{NS}]_{\text{dil}}}{[\text{NS}]_{\text{den}} - [\text{NS}]_{\text{dil}}} \tag{1}$$

In Eq. 1, [NS] is a known quantity, while $[\text{NS}]_{\text{den}}$ and $[\text{NS}]_{\text{dil}}$ correspond to the initially-unknown binodal concentrations of the two phases. Thus, Eq. 1 indicates $[\text{NS}]_{\text{den/dil}}$ can be measured by finding the x-intercept and slope of the ϕ_{den} vs. [NS] line, with the x-intercept giving $[\text{NS}]_{\text{dil}}$ and the slope being equal to the inverse of the difference in binodal concentrations, $[\text{NS}]_{\text{den}} - [\text{NS}]_{\text{dil}}$.

Under all conditions, the x-intercept and slope changed most at temperatures within $\approx 10^{\circ}$C of the onset of phase separation, with further decreases in T leading to no further significant changes. It is possible that, at low temperatures, the system did not fully reach equilibrium due to the NS bond relaxation time growing exponentially as the solution is cooled, which could potentially freeze the dense NS droplet at a certain size, and cause the constant behavior of slope and intercept at low temperatures. However, previous rheology[22] and light scattering[15,24,27,29] experiments show NS networks achieve equilibrium states down to 10°C using cooling rates similar to the ones

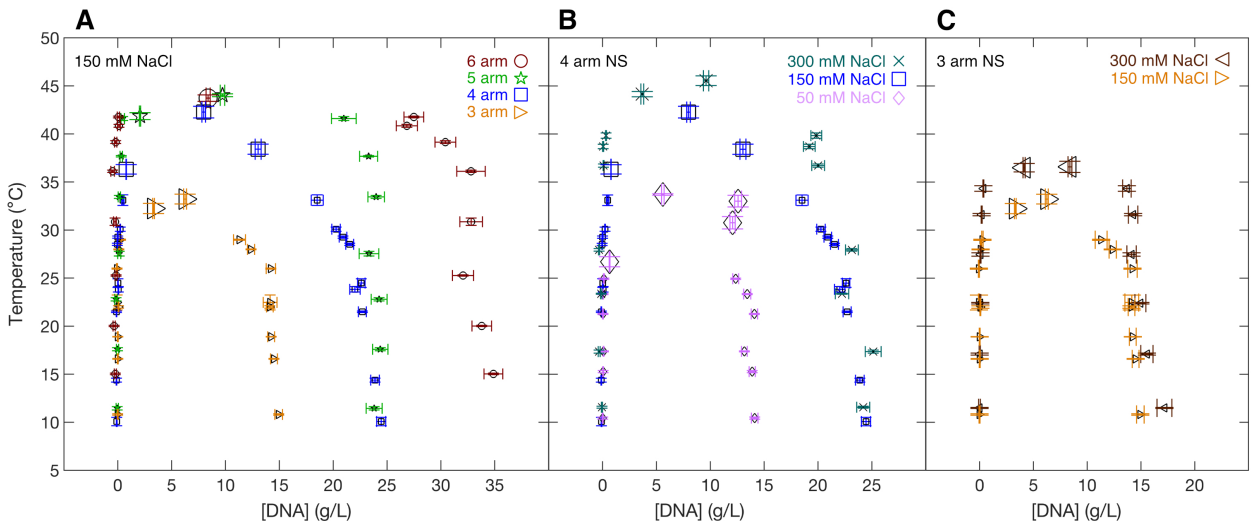

FIG. 3. Temperature-concentration phase diagram of **(A)** NSs of various f, all at [NaCl] = 150 mM, and **(B)** 4-arm and **(C)** 3-arm NS at different [NaCl]. Smaller symbols indicate data found from lever-rule fits (as in Fig. 2), while larger symbols indicate data found from direct melting temperature estimate.

performed here ($\approx$ 0.1 - 1°C/min), suggesting that this behavior is indicative of the equilibrium state of the system.

B. NS phase diagrams

We combined the binodal concentrations measured from lever rule analysis with the melting-temperature measurements to generate temperature-concentration coexistence curves for NSs as a function of arm number, f, and, for $f = 3, 4$ NSs, at various monovalent salt (NaCl) concentrations (Fig. 3). Qualitatively, the diagrams all have a similar shape, demonstrating an upper critical solution temperature, T_c, below which a coexistence regime appears. For $(T_c - T) \lesssim 10°\text{C}$, the coexistence regime increases in width as T decreases, but at lower T the width stabilizes. These features qualitatively match those seen in previous estimates of NS phase diagrams[15].

We sought to quantify T_c so as to facilitate comparison with predictive models. We observed the maximal melting temperature typically occurred at a NS concentration roughly midway between the binodals (Fig. 3). For each NS condition, we took this greatest T_m to be an estimate of T_c, and investigated its variation with other experimental parameters. At constant salt, T_c increased by nearly 10°C from $f = 3$ to $f = 4$, then continued to increase between $f = 4$ and 6, but by only $\sim 2°\text{C}$ (Fig. 4). For 4-arm NSs, and for [NaCl] from 50 mM to 300 mM, T_c increases with salt

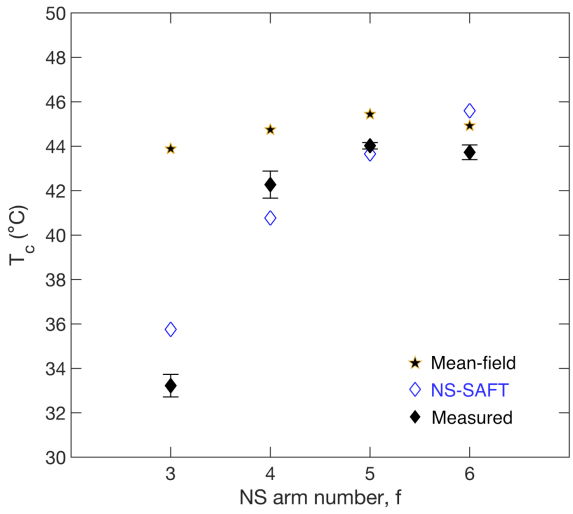

FIG. 4. Critical temperature, T_c, versus NS valence, f, at [NaCl] = 150 mM, as estimated from the experiments (filled black diamonds), the mean-field model (stars), and the NS-SAFT model (empty blue diamonds).

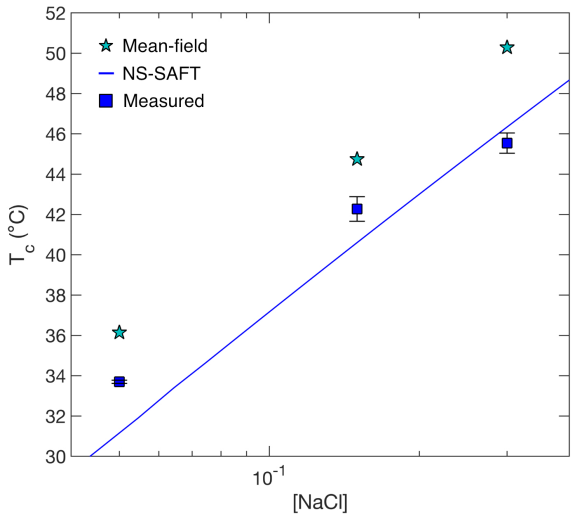

FIG. 5. Semi-log plot of critical temperature, T_c, versus [NaCl] for $f = 4$ NSs, as estimated from the experiments (blue squares), the mean-field model (stars), and the NS-SAFT model (lines).

roughly as $T_c \sim \log[\text{NaCl}]$ (Fig. 5).

The dense-phase binodal concentration, $[\text{NS}]_{\text{den}}$, generally increases with f and [NaCl]. However, there are a few expections where certain pairs of conditions had very similar low-T values of $[\text{NS}]_{\text{den}}$: (i) $f = 4$ vs. $f = 5$ at 150 mM NaCl (Fig. 3A); (ii) $f = 4$ at 150 mM vs. 300 mM NaCl

(Fig. 3B); and (iii) $f = 3$ at 150 mM vs. 300 mM NaCl (Fig. 3C). These are further discussed below.

We found the dilute-phase binodal concentration, $[\mathrm{NS}]_{\mathrm{dil}}$, at lower temperatures to have extremely low values of typically ≤ 0.1 g/L (this is not visible in Fig. 3, but can be seen on a semi-log plot; see supplementary material, Fig. S7). Away from T_c, the binodal roughly traces a $T_m \sim \log([\mathrm{NS}]_{\mathrm{dil}})$ dependence, as also seen in certain models[30]. However, the very low concentration of the dilute NS phase, along with experimental uncertainties (discussed below), means this is not perfectly resolved. Indeed, at the lowest T, these factors sometimes caused a negative x-intercept for the line fitted to lever-rule data (as in Fig. 2), corresponding to a physically-impossible negative value of $[\mathrm{NS}]_{\mathrm{dil}}$.

C. Modeling of phase behavior

We compared the experimental results for T_c to predictions to gain insight into NS LLPS behavior, first through a simple mean-field model. In this picture, we ignored the geometry of the NS, and compared our measurements of T_c to the predicted melting temperatures, T_m, of a solution of *unconnected* (free) oligomers at concentrations corresponding to those of the NS sticky ends, $[\mathrm{oligomer}] = f \cdot [\mathrm{NS}]$). We estimated T_m using the DNA thermodynamics approach of Santa Lucia[31], based on the specific sequence, salt, and oligomer concentration utilized. Particularly, we used the oligomer sequence 5'-ACGATCG-3', which consists of the sticky-end sequence plus a single unpaired base that is also present in the NS structure. We accounted for the effect of the free base using the standard SantaLucia dangle correction[31] and added an empirical "tail" correction to capture the effect of the flanking NS arms on the sticky-end strength[26,32]. The results of this mean-field calculation are plotted in Figs. 4 and 5, which shows the model is in the vicinity of the experimental values, and captures the trend with salt, but fails to account for the large measured variation of T_c with f.

This failure suggests the f-fold connectivity of sticky ends that is enforced by the NS structure plays an important role in determining the LLPS behavior. To capture this, we followed the work of Rovigatti and collaborators[26,30,33], who developed a method for predicting NS phase diagrams using the Statistical Associating Fluid Theory (SAFT) created by Wertheim[34–36] and further developed by Chapman *et. al.*[37–39]. In SAFT, a first-order perturbation calculation is used to construct the free energy of a solution of particles from the free energy of an ideal fluid, with corrections

for repulsive (excluded-volume) interactions, and for f-valent inter-particle binding. Rovigatti *et al.* extended this model to NSs by estimating the excluded volume parameter (*i.e.*, the 2nd virial coefficient), B_2, from coarse-grained molecular dynamics simulations of NSs[30] and by using a temperature-dependent bonding term based on the Santa Lucia model with a tail correction, as noted above.[26,33] The resulting equations can then be solved numerically to directly estimate T_c through the stability constraint that, at the critical point, both the first and second derivatives of the pressure with respect to density are zero.

We used the NS-SAFT approach (Appendix D), adjusted for the specific sticky-end sequence used here, and, for 3- and 4-armed NSs, using B_2 values from Ref.[30]. This prior work did not investigate B_2 values for 5- or 6-armed NSs; since the underlying simulations are quite involved, we opted to estimate their B_2 values by extrapolation from the numerically simulated values for 4 arm NSs. In particular, we posited that the excluded volume should scale with the number of NS arms, i.e. $B_2 \sim f$. Indeed, from the simulated B_2 for 3 and 4 arm NSs[30], we found B_2(4 arm)/B_2(3 arm) $\approx$ 1.43-1.48, which is not too different from 4/3. We accordingly estimated the second virial coefficients for 5 and 6 arm NSs from B_2(5 arm) = (5/4)·B_2(4 arm) and B_2(6 arm) = (6/4)·B_2(4 arm).

Using these B_2 values, we found the NS-SAFT model provides a good description of the variation of T_c with both salt and f (Figs. 4 and 5). Notably, the model is quite close to experiment at at large f, and (unlike the mean-field picture) captures the large decrease in T_c as f decreases to 3.

IV. DISCUSSION

A. Benefits and drawbacks of phase diagram measurement through imaging emulsified phase-separated solutions

We have presented an emulsion-imaging method for quantifying the temperature-concentration phase diagram of LLPS macromolecular solutions. Our results validate the method both in that the measured NS phase diagrams are consistent with prior measurements and predictions[15,21,30], and through our direct confirmation of the applicability of the lever rule (Fig. 2), which is expected to hold based on fundamental thermodynamic and mass-action considerations.

As with other emulsion-based approaches[17–19], the method developed here offers a variety of benefits: First, centrifugation and/or direct handling are not required to assay the dense phase.

Apart from adding processing time, direct handling can be technically difficult for biomolecular liquids, which are high-viscosity, condensed phases that tend to non-specifically adhere to surfaces (*e.g.*, pipette tips, tubes). A further benefit of the method is that it achieves very low sample use by portioning the sample into micron-scale water-in-oil droplets. Also, the ability to simultaneously image multiple emulsion droplets improves measurement precision, since each droplet represents an independent sample, their proximity ensures consistency of temperature, and their small size allows for rapid equilibration. Further, we showed that multiplexing is readily achieved by loading different samples in different channels on a single microscope slide, allowing assay of different solution conditions with a single temperature sweep.

The method is particularly good for resolving the concentration of the dense phase, $[\mathrm{NS}]_{\mathrm{den}}$, based on measuring slope of the lever-rule data (Fig. 2); notably, this is the phase whose properties are traditionally more difficult to assay. In contrast, a drawback was the difficulty in accurate quantification of the dilute binodal. This arose specifically because of the extraordinarily low dilute-phase density of the NS system. Particularly, our measurements of total NS concentration, [NS], carried an uncertainty of, at best ≈ 1 μM, which is ≈ 0.06 g/L for $f = 4$, leading to a similar magnitude of the uncertainty in the best-fit values of the x-intercept in the lever-rule data. However, the values of $[\mathrm{NS}]_{\mathrm{dil}}$ at low T were typically $\lesssim 0.1$ g/L, and thus could not be precisely resolved. A previous article using UV absorbance reported higher values, $[\mathrm{NS}]_{\mathrm{dil}} \approx 0.5$ g/L for $f = 4$, but interpreted those values as being an overestimate due to the presence of malformed NSs[15]. The low values found here for $[\mathrm{NS}]_{\mathrm{dil}}$ are consistent with a recent numerical calculation of the NS phase diagram that found $[\mathrm{NS}]_{\mathrm{dil}} \lesssim 0.1$ g/L under similar conditions[26]. Generally, since the issues in quantifying $[\mathrm{NS}]_{\mathrm{dil}}$ arose from limitations in our measurements of the total NS concentration, rather than a systematic issue with the imaging, the technique should be able to quantify the dilute-solution binodal in systems where it falls at higher concentrations.

We rely on fluorescent labeling to quantify condensate volume fraction, which is then used to estimate the phase diagram. This differs from other fluorescent phase-measurement approaches, in which the absolute fluorescent intensity of each phase is used to estimate concentration[28,40,41]. Using fluorescent intensity requires a separate calibration to relate intensities to concentrations; further, intensity measurements can be complicated by photophysical phenomena, such as quenching interactions amongst dyes, or between dyes and the macromolecule, that affect intensity[42–44]. In contrast, our ϕ-oriented approach is insensitive to absolute intensity, so long as the two phases are bright enough to visualize and to be distinguished. Generally, fluorescent approaches have

the drawback that labelling can be difficult, and can potentially perturb the system's behavior. Accordingly, label-free approaches have been developed to measure phase behavior[42,45], including a recent work that used bright-field images to measure ϕ_{den} of condensates within emulsion droplets[19]. In comparison to that work, a benefit of our approach is the relative simplicity of fluorescent imaging, which allows us to use a mechanistic, quantitative model of the intensity distribution (i.e. the double-sphere function). Further, in fitting that model to the data, we utilize all pixels in the droplet image, including both pixels near the sphere boundaries, and those away from boundaries that carry information on the curvature (and thus radius) of each sphere (see Fig. 1B); this contrasts with the bright-field method that used an edge-detection approach focused on boundaries[19]. Because of this combination of a well-defined intensity profile, and efficient use of all available information, we achieve very low uncertainty (typically $< 1\%$) in our estimate of R, and thus extremely precise estimates of ϕ_{den}. Overall, then, there are benefits and drawbacks to the various methods; we expect the best approach will generally depend on the nature of the system in question.

B. Interpreting NS critical temperatures

Apart from development of the emulsion-imaging method, a second salient output of this work is the phase diagrams themselves, which yield insight into the mechanisms controlling the valence-limited NS system. As noted above, the phase diagrams uniformly show an upper critical solution temperature, consistent with the temperature-destabilized nature of the DNA hybridization bond, and a coexistence regime whose T_c and $[\text{NS}]_{\text{den}}$ increased with monovalent salt and nanostar valence, f.

The salt-dependence of T_c (Fig. 5) can be understood through the electrostatics of DNA hybridization: repulsion between negatively-charged DNA strands is reduced by the screening effect of added salt, causing hybridization strength (and thus T_c) to increase with [salt]. More quantitatively, we note that the differing charge densities of double-stranded and single-stranded DNA means that there is a change in the number of salt ions localized near the DNA when it hybridizes[46], leading to a free energy cost of hybridization related to the chemical potential of the salt, $\mu_{\text{salt}} \sim T \log[\text{salt}]$. This ultimately gives rise to the log[salt] dependence of the measured T_c (Fig. 5). Both the mean-field and NS-SAFT models capture this log[salt] dependence because it is present in the Santa Lucia estimates of DNA thermodynamics[31], whose predictions inform both

models.

The mechanisms underlying the dependence of T_c on f are more involved. Our experimental results show a strong decrease in T_c when f decreases to 3. Simple mean-field pictures fail to account for this behavior, but it is captured by the NS-SAFT model. Interestingly, the mean-field predictions are not very far off for higher valences, which indicates the dominant role in such systems is played by the thermal stability of the DNA bond itself. Yet the mean-field model, in all conditions, predicts transitions at higher temperatures than experimentally observed. This is likely because it overestimates the translational freedom of the bound state (i.e. the model implicitly assumes the bound state is a freely-translating dimer, rather than a condensed DNA network). The failure of the mean-field model emphasizes that bond connectivity (rather than just bond strength) is crucial to the behavior of low-valence NS networks.

In contrast, the NS-SAFT model (adapted here from Rovigatti *et al.*[26,30,33]) includes connectivity, and indeed is generally successful in predicting T_c vs. f, including the large decrease at $f = 3$. However, the NS-SAFT predictions are not perfectly aligned with experiment. At higher valences, it is possible that this is due to the approximation used for the excluded-volume parameter ($B_2 \sim f$), meaning the prediction might be improved by carrying out direct simulations to find $B_2(f = 6)$. But it is also possible that the experiments carry systematic errors that are not accounted for. For example, the method for estimating T_c from melting temperatures is somewhat inexact. Further, it is also possible that sample quality was imperfect: misassembled NSs can result from issues with stoichiometry of the constituent strands, or from errors in the DNA synthesis process, and their presence could affect the measured phase behavior, as noted previously[15].

C. Low-T behavior of condensate density

Our phase diagram measurements indicate that, in a given condition, the coexistence concentration of the dense phase, $[\mathrm{NS}]_{\mathrm{den}}$, tends to rapidly stabilize as T decreases below T_c. This feature was also observed by others[15,26], and has been attributed to the strong (exponential) increase in DNA hybridization strength as temperature decreases– essentially, as T decreases below T_c, the binding energy quickly becomes strong enough to ensure that the number of bonds in the system is maximized; thus further temperature decrease does not lead to more bonds, causing the network density to stabilize. Interestingly, we observed two conditions ($f = 4$ and $f = 3$ at 150 mM NaCl) in which there is a slow variation of $[\mathrm{NS}]_{\mathrm{den}}$ below T_c. Because the exponential depen-

dence of hybridization strength on temperature should still hold, this feature is likely instead due to conformational behaviors and/or structural transitions of the NSs in these conditions.

To gain further insight into the values of NS_{den} at low T, it is useful to establish a metric for comparison. Analogous to Biffi *et al.*[15], we posit that, for the 4- and 6-armed NSs, relevant metrics are the density when arranged into, respectively, diamond and simple-cubic lattices, representing a potential structure for particles with, respectively, 4 and 6 nearest neighbors. We estimate the NS-NS center-to-center distance to be 18.4 nm, if the DNA arms are fully stretched (see supplementary material, Section S2). Then, the density of an $f = 4$ NS diamond lattice is 10.4 g/L, and that of an $f = 6$ simple cubic lattice is 23.2 g/L. The measured low-T values of NS_{den}, for $f = 4$ and $f = 6$, exceed these values. This occurs partially because the entropic elasticity of the DNA arms pulls the particles closer together, and, for $f = 4$, likely due to a tendency for the NSs to adopt planar structures[33]. Generally, dense states are electrostatically unfavorable, as they bring the negatively-charged phosphates along the DNA backbones into close proximity; accordingly, our data show adding salt favors a denser DNA liquid for both $f = 3$ and $f = 4$ NSs, as has been previously observed[21]. That said, we note that the $f = 4$ density at the lowest salt approaches the diamond lattice value, perhaps indicating the high inter-arm electrostatic repulsion in those conditions favors that structure; direct structural analysis would of course be needed to confirm this.

For both $f = 3$ and 4, we found little increase in low-T $[NS]_{den}$ when switching from [NaCl] = 150 mM to 300 mM. This differs from a previous result on $f = 4$ NSs that used a centrifugation assay, and observed a strict monotonic increase in density with salt, though over a slightly different range (250 mM to 1000 mM NaCl)[21]. The discrepancy could be attributed to the differences in the sequence design between the two experiments. Alternatively, we speculate that more complex mechanisms might be relevant, such as the differing effects of electrostatic screening on inter-NS interactions versus intra-NS interactions, e.g at the junction.

The increase in low-T values of $[NS]_{den}$ with valence is expected, since higher-f NSs have both more DNA per particle (e.g. an $f = 6$ particle contains twice as much DNA as an $f = 3$ particle), and because NSs with larger f will tend to have more bound neighbors. Indeed, the $f = 6$ NSs have more than twice the low-T density of the $f = 3$ NSs, which underlines the role of the bound neighbors. However, the near-equivalence of the low-T condensate density between 4 and 5 armed NSs is not consistent with this picture. Intriguingly, a recent rheology experiment observed a similar trend with valence of elasticity[22] as observed here for density: namely, the

modulus of the rubber plateau of NS condensates clearly increased when moving from $f = 3$ to 4 to 6, but the modulus for $f = 5$ was similar to $f = 4$. We speculate that both results are due to the $f = 5$ NS adopting a unique structure in the condensate, relative to the 4- and 6-armed particles, but more work is needed to clarify this.

V. CONCLUSION

We have established a simple method for obtaining the temperature-concentration phase diagram of a liquid-liquid phase separating macromolecular system in which water-in-oil emulsion droplets, at controlled temperature, are imaged with a low-magnification, low-NA fluorescence microscope. The method offers various advantages, including no direct handling of the dense state, low sample-volume use, and precise extraction of condensate volume fraction. The method is readily applied to other macromolecular systems that can be fluorescently labeled. Here, we applied it to the study of LLPS exhibited by multivalent DNA NSs, finding strong effects of particle valence and salt concentration on the phase diagram. The results confirm predictions of the NS-SAFT numerical model, and generally give insight into limited-valence phase separation.

ACKNOWLEDGMENTS

We thank Lorenzo Rovigatti and Emanuele Locatelli for supplying the simulated second-virial coefficient data for $f = 3$ and 4 NS, and for insightful discussions about NS-SAFT calculations. We also thank Patrick McCall for helpful conversations. This project was supported by the National Science Foundation under Award No. CMMI 1935400.

DATA AVAILABILITY STATEMENT

The data that support the findings of this study are available from the corresponding authors upon reasonable request.

Appendix A: NS, Hairpin, and emulsion preparation

HPLC purified DNA oligomers were purchased in a dehydrated state from IDT, and hydrated with MilliQ water to form stocks with concentrations of $500 - 800$ μM. All DNA sequences used

in this experiment are listed in the Table S1 of the supplementary material. The sequences used for NS-forming oligomers followed prior work[22]. The sequence of the hairpin-forming oligomer was designed to lack any hybridization with NS sticky ends, and to have a folding (melting) temperature similar to that of the NS arms ($\approx 80^{\circ}$C).

To assemble an f-armed NS, f constituent oligomers were mixed in a buffer of 40 mM Tris, 11 mM HCl, 1mM EDTA containing either 50, 150, or 300 mM NaCl. In this mixture, 5% of one of the strands was labeled with Cy3 (see Table S1). For $f = 6$ assemblies, achieving the desired stock concentration required complete dehydration, followed by re-hydration in buffer with 150 mM NaCl. These NS mixtures were then thermally annealed following the protocol detailed in Ref.[22]. Separately, the hairpin oligomer was diluted with the relevant buffer and salt, and annealed it using the same procedure. Final measurement solutions were then made by mixing annealed NS and annealed hairpin, with a hairpin concentration of typically 5 μM; notably, controls indicated that varying [hairpin] from 0.5 μM to 20 μM had no effect on the volume fraction of the dense NS phase (see supplementary material, Fig. S3). NS concentration was found from these NS+hairpin mixtures by diluting to a 1% solution with added water, melting, measuring the UV absorbance (A260), subtracting the A260 of the hairpin (as measured separately from the hairpin stock), and then estimating the NS oligomer concentration using sequence-dependent estimates of the extinction coefficients[47].

Water-in-oil emulsions were made at $T = 65^{\circ}$C by delivering 2-3 μL of the NS+hairpin solutions into 40 μL of a mixture of 5% wt/wt fluorinated-surfactant dissolved in a fluorinated oil (008 FluoroSurfactant in HFE7500 oil, RAN Biotechnologies). The solution was held at 60-65°C for 1-2 minutes to disallow phase separation, then emulsified by vortexing for 2-3 seconds at an intensity of roughly an eighth of the maximum on a Benchmark Benchmixer vortexer. This resulted in droplets of the desired diameter ($25 - 120$ μm).

Appendix B: Imaging protocol

Multi-channel flow cells were created by cutting two vinyl sheets (Cricut Window Cling) with a personal die cutting machine (Cricut Joy). One sheet contained an array of small holes for catching air bubbles, and the second contained an array of channels. The bubble-catching sheet was placed on an ethanol-cleaned glass slide, and pressed and heated to create adhesion. The channel sheet was aligned to the first sheet, adhered through heat and pressure, and finally a cleaned 22x50 mm

coverslip was similarly adhered to complete the flow cell.

Images were acquired using a 4x 0.13 NA objective (Olympus UPlan FL) on an inverted, wide-field, fluorescent microscope (Olympus IX70), illuminated with a mercury arc lamp that was attenuated with a 1.0 ND filter. A subset of images were taken with two different 4x 0.1 NA objectives (Olympus Plan N or Nikon Plan Achromat). Fluorescence imaging was achieved using a 540 ± 30 nm bandpass excitation filter (540AF30 Omega), a 570 nm long-pass dichroic (570DRLP Omega) and a 585 ± 40 nm bandpass filter (HQ585/40 Chroma). Images were captured with a CCD camera (Hamamatsu Orca-R2 C10600) and saved to a computer using the camera's imaging software (HCImage Live).

Temperature was controlled by placing on top of the flow cell a brass heat block through which water was circulated using an external water bath (Neslab refrigerated circulating bath RTE-8). The flow-cell slide and heat block were insulated by a home-made styrofoam casing when imaging. Temperature was recorded using a type-K digital thermometer (Supco SL500TC) outfitted with a thermocouple probe (1.6 mm bead diameter) that was taped between the heat block and flow-cell slide.

Emulsified NS solutions of different [NS] were loaded into distinct channels of the flow cell, heated to dissolve any condensate, then allowed to equilibrate and settle over hours. The flow cell was then placed on the stage, in contact with the brass block, which was set to the high end of the desired temperature range. The system was allowed to equilibrate for 5-10 minutes, then imaged. Data at subsequent temperatures was acquired by repeating the sequence of temperature change/equilibrate/image.

Appendix C: Imaging analysis

Images of the emulsified NS+hairpin solutions were first manually processed using FIJI to remove any artifacts (e.g. droplet clusters or visible contaminants), then imported into a custom analysis code written in Mathematica. In that code, the function *ComponentMeasurements* was used to automatically find droplets of the desired size ($25-120\ \mu$m diameter) that were sufficiently separated from other droplets. The relevant droplet images were then cropped and fit to the double-sphere function (see supplementary material, Eq. S1-3) using the *NonlinearModelFit* function. The fitting parameters were used to calculate ϕ_{den}.

Appendix D: NS-SAFT calculations

The free energy of each NS system were calculated as defined by the NS-SAFT theory detailed in Reference[26] (equations (1-2) and (6-9) in their paper). From the calculated free energy, the critical temperature was found by numerically solving equation 10 in Reference[26] using the *FindRoot* function in Mathematica.

REFERENCES

[1]H. R. Kruyt and H. G. Bungenberg de Jong, "Zur kenntnis der lyophilen kolloide," Kolloidchemische Beihefte **28**, 1–54 (1928).

[2]R. J. Stewart, J. C. Weaver, D. E. Morse, and J. H. Waite, "The tube cement of phragmatopoma californica: a solid foam," Journal of Experimental Biology **207**, 4727–4734 (2004).

[3]J. H. Waite, N. H. Andersen, S. Jewhurst, and C. Sun, "Mussel adhesion: Finding the tricks worth mimicking," The Journal of Adhesion **81**, 297–317 (2005).

[4]C. P. Brangwynne, T. J. Mitchison, and A. A. Hyman, "Active liquid-like behavior of nucleoli determines their size and shape in xenopus laevis oocytes," PNAS **108**, 4334–4339 (2010).

[5]D. Bracha, M. T. Walls, M.-T. Wei, L. Zhu, M. Kurian, J. Avalos, J. E. Toettcher, and C. P. Brangwynne, "Mapping local and global liquid phase behavior in living cells using photo-oligomerizable seeds," Cell **175**, 1467–1480 (2018).

[6]K. Rippe, "Liquid–liquid phase separation in chromatin," Cold Spring Harbor Perspectives in Biology (2021).

[7]J.-K. Ryu, D.-E. Hwang, and J.-M. Choi, "Current understanding of molecular phase separation in chromosomes," International Journal of Molecular Sciences **22**, 10736 (2021).

[8]R. A. Jain, "The manufacturing techniques of various drug loaded biodegradable poly(lactide-co-glycolide) (plga) devices," Biomaterials **21**, 2475–2490 (2000).

[9]C. Luebbert, F. Huxoll, and G. Sadowski, "Amorphous-amorphous phase separation in api/polymer formulations," Molecules **22**, 1–17 (2017).

[10]C. Luebbert, E. Stoyanov, and G. Sadowski, "Phase behavior of asds based on hydroxypropyl cellulose," International Journal of Pharmaceutics: X **3**, 100070 (2021).

[11]D. Eratte, B. Wang, K. Dowling, C. J. Barrow, and B. P. Adhikari, "Complex coacervation with whey protein isolate and gum arabic for the microencapsulation of omega-3 rich tuna oil," Food

& Function **5**, 2743–2750 (2014).

[12]Z. Xiao, W. Liu, G. Zhu, R. Zhou, and Y. Niu, "A review of the preparation and application of flavour and essential oils microcapsules based on complex coacervation technology," Journal of the Science of Food and Agriculture **94**, 1482–1494 (2014).

[13]S. Alberti, A. Gladfelter, and T. Mittag, "Considerations and challenges in studying liquid-liquid phase separation and biomolecular condensates," Cell **176**, 419–434 (2019).

[14]Y. Luo, M. Gu, C. E. Edwards, M. T. Valentine, and M. E. Helgeson, "High-throughput microscopy to determine morphology, microrheology, and phase boundaries applied to phase separating coacervates," Soft Matter **18**, 3063–3075 (2022).

[15]S. Biffi, R. Cerbino, F. Bomboi, E. M. Paraboschi, R. Asselta, F. Sciortino, and T. Bellini, "Phase behavior and critical activated dynamics of limited-valence dna nanostars," PNAS **110**, 15633–15637 (2013).

[16]K. A. Black, D. Priftis, S. L. Perry, J. Yip, W. Y. Byun, and M. Tirrell, "Protein encapsulation via polypeptide complex coacervation," ACS Macro Letters **3**, 1088–1091 (2014).

[17]S. Deshpande and C. Dekker, "Studying phase separation in confinement," Current Opinion in Colloid & Interface Science **52**, 101419 (2021).

[18]A. Hensley, W. M. Jacobs, and W. B. Rogers, "Self-assembly of photonic crystals by controlling the nucleation and growth of dna-coated colloids," Proc Natl Acad Sci U S A **119** (2022), 10.1073/pnas.2114050118.

[19]A. Villois, U. Capasso Palmiero, P. Mathur, G. Perone, T. Schneider, L. Li, M. Salvalaglio, A. deMello, S. Stavrakis, and P. Arosio, "Droplet microfluidics for the label-free extraction of complete phase diagrams and kinetics of liquid–liquid phase separation in finite volumes," Small **n/a**, 2202606 (2022).

[20]D. C. Johnston, in *Advances in Thermodynamics of the van der Waals Fluid* (Institute of Physics Publishing, 2014).

[21]B.-j. Jeon, D. T. Nguyen, G. R. Abraham, N. Conrad, D. K. Fygenson, and O. A. Saleh, "Salt-dependent properties of a coacervate-like, self-assembled dna liquid," Soft Matter **14**, 7009–7015 (2018).

[22]N. Conrad, T. Kennedy, D. K. Fygenson, and O. A. Saleh, "Increasing valence pushes dna nanostar networks to the isostatic point," PNAS **116**, 7238–7243 (2019).

[23]F. Bomboi, S. Biffi, R. Cerbino, T. Bellini, F. Bordi, and F. Sciortino, "Equilibrium gels of trivalent dna-nanostars: Effect of the ionic strength on the dynamics," The European physical

journal E. Soft Matter **38** (2015).

[24]S. Biffi, R. Cerbino, G. Nava, F. Bomboi, F. Sciortino, and T. Bellini, "Equilibrium gels of low-valence dna nanostars: a colloidal model for strong glass former," Soft Matter **11**, 3132–3138 (2015).

[25]G. Nava, M. Rossi, S. Biffi, F. Sciortino, and T. Bellini, "Fluctuating elasticity mode in transient molecular networks," Phys. Rev. Lett. **119**, 078002–7 (2017).

[26]L. Rovigatti and F. Sciortino, "An accurate estimate of the free energy and phase diagram of all-dna bulk fluids," Polymers **10**, 447 (2018).

[27]E. Lattuada, D. Caprara, R. Piazza, and F. Sciortino, "Spatially uniform dynamics in equilibrium colloidal gels," Science Advances **7** (2021).

[28]T. Lee, S. Do, J. G. Lee, D.-N. Kim, and Y. Shin, "The flexibility-based modulation of dna nanostar phase separation," Nanoscale **13**, 17638–17647 (2021).

[29]L. Rovigatti, F. Smallenburg, F. Romano, and F. Sciortino, "Gels of dna nanostars never crystallize," ACS Nano **8**, 3567–3574 (2014).

[30]E. Locatelli, P. H. Handle, C. N. Likos, F. Sciortino, and L. Rovigatti, "Condensation and demixing in solutions of dna nanostars and their mixtures," ACS Nano **11**, 2094–2102 (2017).

[31]J. SantaLucia and D. Hicks, "The thermodynamics of dna structural motifs," Annual Review of Biophysics and Biomolecular Structure **33**, 415–440 (2004).

[32]L. Di Michele, B. M. Mognetti, T. Yanagishima, P. Varilly, Z. Ruff, D. Frenkel, and E. Eiser, "Effect of inert tails on the thermodynamics of dna hybridization," Journal of the American Chemical Society **136**, 6538–6541 (2014).

[33]L. Rovigatti, F. Bomboi, and F. Sciortino, "Accurate phase diagram of tetravalent dna nanostars," The Journal Of Chemical Physics **140**, 154903 (2014).

[34]M. Wertheim, "Fluids with highly directional attractive forces. i. statistical thermodynamics," Journal of Statistical Physics **35**, 19–34 (1984).

[35]M. Wertheim, "Fluids with highly directional attractive forces. ii. thermodynamic perturbation theory and intergral equations," Journal of Statistical Physics **35**, 35–47 (1984).

[36]M. Wertheim, "Fluids with highly directional attractive forces. iii. multiple attraction sites," Journal of Statistical Physics **42**, 459–476 (1986).

[37]W. G. Chapman, G. Jackson, and K. E. Gubbins, "Phase equilibria of associating fluids," Molecular Physics **65**, 1057–1079 (1988).

[38]W. G. Chapman, K. E. Gubbins, G. Jackson, and M. Radosz, "New reference equation of state for associating liquids," Industrial & Engineering Chemistry Research **29**, 1709–1721 (1990).

[39]W. Zmpitas and J. Gross, "Detailed pedagogical review and analysis of wertheim's thermodynamic perturbation theory," Fluid Phase Equilibria **428**, 121–152 (2016).

[40]S. Alberti, S. Saha, J. B. Woodruff, T. M. Franzmann, J. Wang, and A. A. Hyman, "A user's guide for phase separation assays with purified proteins," Journal of Molecular Biology **430**, 4806–4820 (2018).

[41]S. Choi, M. O. Meyer, P. C. Bevilacqua, and C. D. Keating, "Phase-specific rna accumulation and duplex thermodynamics in multiphase coacervate models for membraneless organelles," Nature Chemistry **14**, 1110–1117 (2022).

[42]Y. Hong, K. P. Dao, T. Kim, S. Lee, Y. Shin, Y. Park, and D. S. Hwang, "Label-free quantitative analysis of coacervates via 3d phase imaging," Advanced Optical Materials **9**, 2100697 (2021).

[43]V. C. Coffman and J. Q. Wu, "Counting protein molecules using quantitative fluorescence microscopy," Trends Biochem Sci **37**, 499–506 (2012).

[44]T. Kekic and J. Lietard, "Sequence-dependence of cy3 and cy5 dyes in 3' terminally-labeled single-stranded dna," Scientific Reports **12**, 14803 (2022).

[45]P. M. McCall, K. Kim, A. W. Fritsch, J. Iglesias-Artola, L. Jawerth, J. Wang, M. Ruer, J. Peychl, A. Poznyakovskiy, J. Guck, S. Alberti, A. A. Hyman, and J. Brugués, "Quantitative phase microscopy enables precise and efficient determination of biomolecular condensate composition," bioRxiv , 2020.10.25.352823 (2020).

[46]D. R. Jacobson and O. A. Saleh, "Counting the ions surrounding nucleic acids," Nucleic Acids Research **45**, 1596–1605 (2016).

[47]M. J. Cavaluzzi and P. N. Borer, "Revised uv extinction coefficients for nucleoside-5'-monophosphates and unpaired dna and rna," Nucleic Acids Res **32**, e13 (2004).